

ARTICLE OPEN

A three-dimensional polyhedral unit model for grain boundary structure in fcc metals

Arash Dehghan Banadaki ¹ and Srikanth Patala ¹

One of the biggest challenges in developing truly bottom-up models for the performance of polycrystalline materials is the lack of robust quantitative structure–property relationships for interfaces. As a first step in analyzing such relationships, we present a polyhedral unit model to classify the geometrical nature of atomic packing along grain boundaries. While the atomic structure in disordered systems has been a topic of interest for many decades, geometrical analyses of grain boundaries has proven to be particularly challenging because of the wide range of structures that are possible depending on the underlying macroscopic crystallographic character. In this article, we propose an algorithm that can partition the atomic structure into a connected array of three-dimensional polyhedra, and thus, present a three-dimensional polyhedral unit model for grain boundaries. A point-pattern matching algorithm is also provided for quantifying the distortions of the observed grain boundary polyhedral units. The polyhedral unit model is robust enough to capture the structure of high- Σ , mixed character interfaces and, hence, provides a geometric tool for comparing grain boundary structures across the five-parameter crystallographic phase-space. Since the obtained polyhedral units circumscribe the voids present in the structure, such a description provides valuable information concerning segregation sites within the grain boundary. We anticipate that this technique will serve as a powerful tool in the analysis of grain boundary structure. The polyhedral unit model is also applicable to a wide array of material systems as the proposed algorithm is not limited by the underlying lattice structure.

npj Computational Materials (2017)3:13 ; doi:10.1038/s41524-017-0016-0

INTRODUCTION

Grain boundaries influence a wide array of properties in polycrystalline materials,¹ including diffusivity,^{2–4} conductivity,^{5–7} intergranular cracking,⁸ corrosion resistance,^{9, 10} embrittlement^{11, 12} etc. However, there remain fundamental challenges in our ability to compute the structure–property relationships of individual interfaces and to analyze the influence of a collection of grain boundaries (GBs) on the macroscopic properties of materials.^{13, 14} Even from a modeling perspective, the ability to develop reliable GB structure–property relationships has been identified as one of the biggest obstacles in developing robust bottom-up models for predicting polycrystalline material behavior.¹⁵ In this article, in an attempt to provide a basis for GB structure–property relationships, we present an automated algorithm to compute the three-dimensional (3D) polyhedral unit model for describing the atomistic structure of GBs in fcc metallic systems.

Defects in crystalline materials may be visualized as local disruptions in the symmetric arrangement of atoms. For example, a point defect corresponds to a missing or an extra atom in the lattice and a line defect is the termination of an extra plane of atoms, which locally disrupts the lattice structure. Investigating the distortions caused by these defects and the analysis of atomic packing along these defects has led to a mechanistic understanding of their influence on material properties.^{16, 17} In a similar vein, it is anticipated that a quantitative understanding of the atomistic structure of GBs will offer fundamental insights into their properties, and will help reduce the complexity of the five-

dimensional crystallographic phase space.¹⁸ For example, it has been proposed that an analysis of GB structures at the atomistic length scale will help classify interfaces as singular, vicinal, and general.¹⁹ Such a classification is expected to lead to a general understanding of the trends by which GB properties change, as the crystallographic parameters of the GBs are varied.²⁰

From a geometrical perspective, the earliest models for interface structures include the “amorphous cement” model²¹ and the sharp interface model with GB atoms on the coincident sites.²² However, GBs generally exhibit a wide range of structures and the extent of “ordering” depends on the density of coincidence lattice points and the symmetry of the boundary-plane (BPI) orientation. Therefore, the atomic structure of GBs has primarily been visualized as clusters of atoms that form certain geometrical motifs. This model, referred to as the structural unit (SU) model, was first proposed by Bishop and Chalmers²³ and has been extended to a variety of tilt configurations by Sutton and Vitek.^{24, 25} However, as described in ref. 26, the SU model is applicable only for pure tilts along low-index rotation axes.

A more general model for the atomic structure description is the 3D polyhedral unit model, proposed by Ashby *et al.*,²⁷ where GB atoms are represented by an array of closed packed polyhedral motifs. This model was inspired by Bernal’s seminal effort in classifying the atomic structure of liquids as an arrangement of polyhedral units.²⁸ These polyhedra, which correspond to the canonical Bernal holes, were identified using models of dense random packing of hard spheres.²⁹ The set of canonical holes and the corresponding polyhedra are shown in Fig. S1 of

¹Department of Materials Science and Engineering, North Carolina State University, Raleigh, NC, USA
Correspondence: Srikanth Patala (spatala@ncsu.edu)

Received: 24 March 2016 Revised: 16 February 2017 Accepted: 28 February 2017
Published online: 27 March 2017

the [Supplementary Information](#). Such a classification of atomic structure through the analysis of voids has also been applied to the structural analysis of mono-atomic metallic glasses.³⁰

Ashby *et al.*²⁷ have utilized this concept to describe the structure of simulated GBs, which primarily included the [100] [110], and [111] symmetric tilt GBs.^{31–33} Through the analysis of these GB structures, Ashby *et al.* proposed a set of polyhedra, termed as deltahedra (densely packed polyhedral units with equilateral triangles for faces; shown in Fig. S1), that may be commonly observed in the GBs of fcc and bcc crystal structures. The primary utility of the polyhedral unit model is believed to be in predicting segregation sites for small interstitial solute atoms.³⁴ For example, Zhou *et al.*³⁵ have recently utilized the polyhedral unit model to predict the segregation sites and compute the energetics of hydrogen segregation in $\Sigma 5(310)$ Nickel GB. The polyhedral unit model is also anticipated to provide a basis for analyzing GB structures of complex crystallography (i.e., high- Σ misorientation, and with both twist and tilt character). However, a major obstacle in using this model is the difficulty associated with automatically identifying polyhedra in a quasi-3D structure of atoms in GBs.

In this article, we describe an automated algorithm to identify the voids and the corresponding polyhedral structure of GBs in fcc metallic systems. In section Polyhedral unit model, we describe the method used to cluster the vertices in a Voronoi network (i.e., the Voronoi-vertices) and describe how the clusters of Voronoi-vertices will result in the identification of the polyhedral unit structure of the GBs. In the Results section, we provide several examples illustrating how the proposed algorithm can successfully describe the structure of symmetric tilt GBs, asymmetric tilt GBs, a symmetric twist GB, a and two mixed character GBs. We leverage a database of hard-sphere packings, provided by Holmes-Cerfon,³⁶ for classifying the geometries of the observed GB polyhedral units.

Polyhedral unit model

The identification of the polyhedral unit structure for a set of atoms is non-trivial as there exist infinitely many solutions that partition the space, occupied by a set of points, into polyhedral units. One of the possible solutions is the Delaunay triangulation of the 3D set of atoms, which results in a complete partitioning of the space into (irregular) tetrahedra. The approach we utilize to compute the polyhedral unit structure is to analyze the voids in the GB structure. The property that may be directly linked to the quantification of the void structure is the segregation of small interstitial solute atoms to GBs. There is also considerable evidence that the free-volume plays a crucial role in influencing a variety of properties in metallic glasses.^{37, 38} As GBs are, in general, more disordered than ordered, we anticipate that a polyhedral unit structure based on the analysis of the void structure will be very useful.

Identification of polyhedral units. The analysis of the cavities in dense random packing of spheres has been well established (e.g., see ref. 39 and references therein). In all of these studies, the cavities are identified by first constructing the Voronoi tessellation of the collection of atoms. The Voronoi polyhedra, VP_i , corresponding to each atom i , partition the 3D space of atoms into distinct domains such that every point in the polyhedron VP_i is closest to atom i than any other atom. Each vertex in the Voronoi network is shared by at least four Voronoi polyhedra (whose atoms construct the Delaunay tetrahedron). The Voronoi vertex is the center of the sphere that circumscribes the Delaunay tetrahedron. Therefore, at each Voronoi vertex (VV) an interstitial atom may be placed and a corresponding radius r_{vv} , of the largest sphere (denoted as VV-sphere in this article) that fits in the void, may be defined. The radius of the VV-sphere depends on the radius of the atoms r_a in the system. If R_{vv} is the radius of the circumsphere (or the distance

between the Voronoi vertex and the atoms of the Delaunay tetrahedron), then the radius of the VV-sphere is $r_{vv} = R_{vv} - r_a$.

For example, for the Bernal's canonical holes and their corresponding polyhedra, shown in Fig. S1, the Voronoi vertices and the VV-spheres are illustrated. It is clear from Fig. S1 that there exists an overlap between the different VV-spheres that are present in the canonical Bernal holes. We use this property of the VV-spheres to combine Delaunay tetrahedra to form larger polyhedral units. As discussed earlier, each Voronoi vertex corresponds to a unique tetrahedron. Therefore, the problem of combining tetrahedra may be formulated alternatively as combining (or as the clustering of) Voronoi vertices, where each cluster results in a polyhedral unit.

The clustering algorithm combines the Voronoi vertices whose VV-spheres overlap, i.e., the vertex VV^i belongs to a cluster C if there exists another vertex $VV^j \in C$, such that $\|VV^i - VV^j\| \leq r_{vv}^i + r_{vv}^j$, where r_{vv}^i and r_{vv}^j are the radii of the VV-spheres at VV^i and VV^j , respectively. This algorithm will cluster all the vertices in the Voronoi network into disjoint sets. The polyhedral units are then computed by combining all the Delaunay tetrahedra of the Voronoi vertices present in each cluster.

To demonstrate the clustering technique, we start with a simple example and illustrate how the proposed algorithm will lead to the detection of the well-established octahedra and tetrahedra in a single crystal fcc structure. Figure 1a(i) shows a super-cell of an fcc crystal extracted from an infinite lattice. The first step in the above algorithm is to find the Voronoi vertices and their corresponding radii. If the lattice parameter is denoted by a , the atom radius is given by $r_a = a/(2\sqrt{2})$. The Voronoi vertices are obtained by constructing the Voronoi tessellation of the fcc lattice and are represented as red stars in Fig. 1a(ii). For each vertex, the radius of the VV-sphere r_{vv} is computed. From these computations, two types of Voronoi vertices are identified. The first type is the vertex with a radius $r_{vv} = r_a(\sqrt{2} - 1) \sim 0.414r_a$, which corresponds to the octahedral interstitial site in an fcc crystal (e.g., the vertex located at $(a/2, a/2, a/2)$). The second type is the vertex with $r_{vv} = r_a(\sqrt{3}/2 - 1) \sim 0.225r_a$, which corresponds to the tetrahedral interstitial site (e.g., the vertex located at $(a/4, a/4, a/4)$). These two types of Voronoi-spheres are shown in Fig. 1a(iii). The distance between these two vertices is $r_a\sqrt{3}/2 \sim 1.2247r_a$, which is greater than the sum of the radii of the Voronoi vertices in the octahedral and the tetrahedral site, i.e., $r_a\sqrt{3}/2 > r_a(\sqrt{3}/2 + \sqrt{2} - 2)$.

Therefore, none of the VV-spheres overlap with each other and the vertices will not cluster together. Put differently, each cluster contains only one vertex and two types of polyhedral units (the octahedron and the tetrahedron as shown in Fig. 1a(iv)) are obtained by identifying the atoms that correspond to each of the Voronoi vertices in the lattice. In this example, the Voronoi-vertices at the octahedral and the tetrahedral sites are created by the atoms that make the octahedron and the tetrahedron, respectively.

Additionally, we test the applicability of the proposed clustering algorithm for identifying the polyhedral unit structure of an fcc crystal with a vacancy. For this purpose, we have constructed a simulation box with five aluminum fcc super-cells along each dimension (125 unit-cells in total) and removed a single atom from the center of the simulation box. The vacancy point defect is then relaxed using the conjugate gradient minimization in LAMMPS⁴⁰ and is shown in Fig. 1b(i). Mishin's EAM potential⁴¹ is used for these computations. The Voronoi vertices within the single crystal region do not overlap and, hence, result in the usual tetrahedra and octahedra. Within the vacancy, a single Voronoi-vertex is observed and the VV-sphere is shown in Fig. 1b(ii). The atoms that correspond to this VV-sphere are those that surround the vacancy and the polyhedron that is obtained by considering all of these atoms together is the cuboctahedron

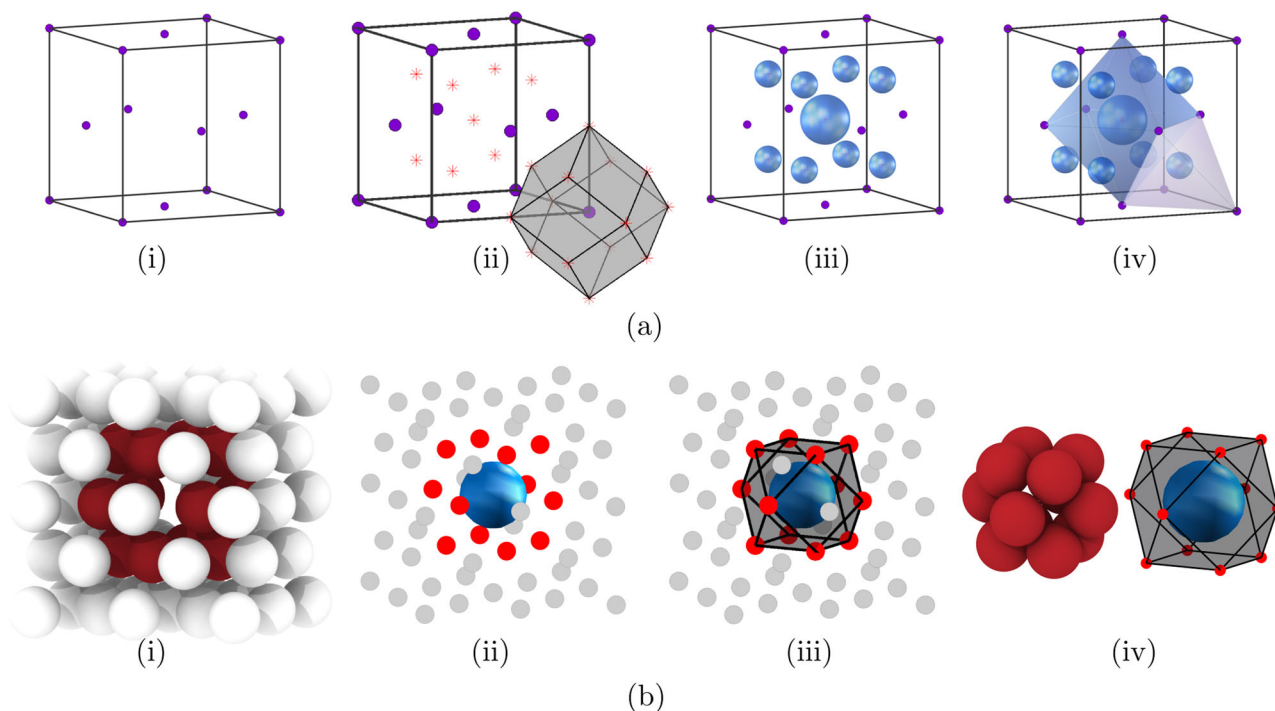


Fig. 1 The Voronoi vertex clustering algorithm for identifying the polyhedral unit structure of **a** an fcc single-crystal region and **b** a vacancy point defect is illustrated. In **a(i)**, the unit cell of an fcc lattice is provided and in **a(ii)**, the Voronoi polyhedron of one of the atoms is shown. Also highlighted are the Voronoi vertices, obtained by constructing the Voronoi polyhedra of all the atoms in the system. In **a(iii)**, the VV-spheres that fall within the unit cell are shown. In **a(iv)**, the octahedron and tetrahedron corresponding to the two distinct types of VV-spheres are depicted. In the case of the vacancy, in **b(i)**, the fcc lattice is shown and the atoms surrounding the vacancy are highlighted. In **b(ii)**, the VV-sphere that is located within the vacancy is illustrated and the atoms that have contributed to the creation of this sphere are highlighted in red. These atoms are the same as those surrounding the vacancy in **b(i)**. The polyhedron that is obtained by triangulating the atoms in **b(iii)** is the cuboctahedron, which is identified as the polyhedral unit model of a vacancy in the fcc lattice

(shown in Fig. 1b(iii)). Therefore, this algorithm automatically identifies the polyhedral unit structure that corresponds to a vacancy in an fcc lattice.

Polyhedral Unit Model for the Symmetric Tilt $\Sigma 5(0\bar{2}1)$ GB. To illustrate the applicability of the VV clustering algorithm for determining the polyhedral unit structure of a GB, we start with the analysis of a simple [100] symmetric tilt $\Sigma 5(0\bar{2}1)$ GB (in section S2, the complete crystallographic information, i.e., the Σ -number, and the Miller indices of the boundary-plane in the two crystals $(hkl)_1$ and $(hkl)_2$, are provided for all the GBs analyzed in this article). This interface is chosen as it illustrates all the steps required for classifying the polyhedral unit model. The atomistic structure of this GB is shown in Fig. 2a. The VV-spheres centered at the Voronoi vertices of the atomistic structure of the GB are shown in Fig. 2b(i, ii). Using the clustering algorithm, the clusters of the Voronoi vertices, whose spheres overlap, are identified. A representative example of the polyhedral units, obtained by combining the Delaunay tetrahedra of all the Voronoi vertices in each cluster, is shown in Fig. 2c(i). For $\Sigma 5(0\bar{2}1)$ GB, the atomistic structure consists of a stacking of polyhedra, each containing thirteen atoms, as shown in Fig. 2d(i, ii). Therefore, the 13-atom polyhedral unit, shown explicitly in Fig. 2c(i), completely describes the 3D structure of the $\Sigma 5(0\bar{2}1)$ GB.

Once the polyhedra are extracted from the GB, it is necessary to classify the units according to their geometry. As will be described in this article, the database of possible geometrical motifs cannot be classified using the simple polyhedral units proposed by Bernal²⁹ or Ashby *et al.*²⁷ In order to capture the complexity of the various polyhedral units that may be observed in general GBs, a new database of geometrical motifs, derived from the rigid hard-sphere packings and enumerated by Holmes-Cerfon,³⁶ is utilized.

The rigid hard-sphere packings can be classified as either iterative or seed clusters. Seeds are n -atom packings that cannot be constructed out of rigid packings of less than n atoms, i.e., they contain within them an inherently new structure. An exhaustive list of seeds with $n = 4, 6, 7, 8, 9, 10, 11$ atoms are shown in Figs. S1 and S2 of the Supplementary Information. On the other hand, iterative packings are those that can be obtained by joining smaller seed clusters.

The process of analyzing the observed GB units involves finding the model-unit (from the Holmes-Cerfon database) that best matches the GB polyhedron. The algorithm required for comparing polyhedral units is described in section S3.1. If the best-match unit is iterative, then the unit is split into seed clusters resulting in GB polyhedral units that correspond only to seeds (e.g., refer to Fig. S5). Hence, the seed units constitute the database of canonical models for the observed GB polyhedra. While this process is, in principle, sufficient for classifying all the observed GB polyhedral units, it is not entirely efficient. This is due to the fact that the total number of rigid hard-sphere packings increases as a factorial function ($\sim 2.5(n-5)!$) of the number of atoms n (Table S2). Therefore, an additional processing step is introduced to reduce the size of the observed GB polyhedral units with more than 12 atoms.

Very briefly, if the observed polyhedron contains more than 12 atoms and it is convex, then the unit is minimized in LAMMPS and the minimized structure is deemed as the canonical model of the polyhedral unit. However, if the unit is concave, the unit is split into smaller units that define the interstitial sites⁴² in the polyhedral unit. The interstitial voids correspond to the largest non-overlapping VV-spheres. In order to obtain all the interstitial voids in the unit, the voids are first sorted according to their sizes. Then the largest VV-sphere is picked and clustered with the

VV-spheres, remaining in the list, that it overlapped. The cluster with the largest VV-sphere and its overlapping VV-spheres correspond to one interstitial site. The list of VV-spheres is updated by removing the cluster of VV-spheres of the interstitial

site obtained in the previous step and the process is repeated until all the VV-spheres are exhausted in the list and all the interstitial sites enumerated. This post-processing step is described in complete detail, with examples, in section S3.2. To summarize,

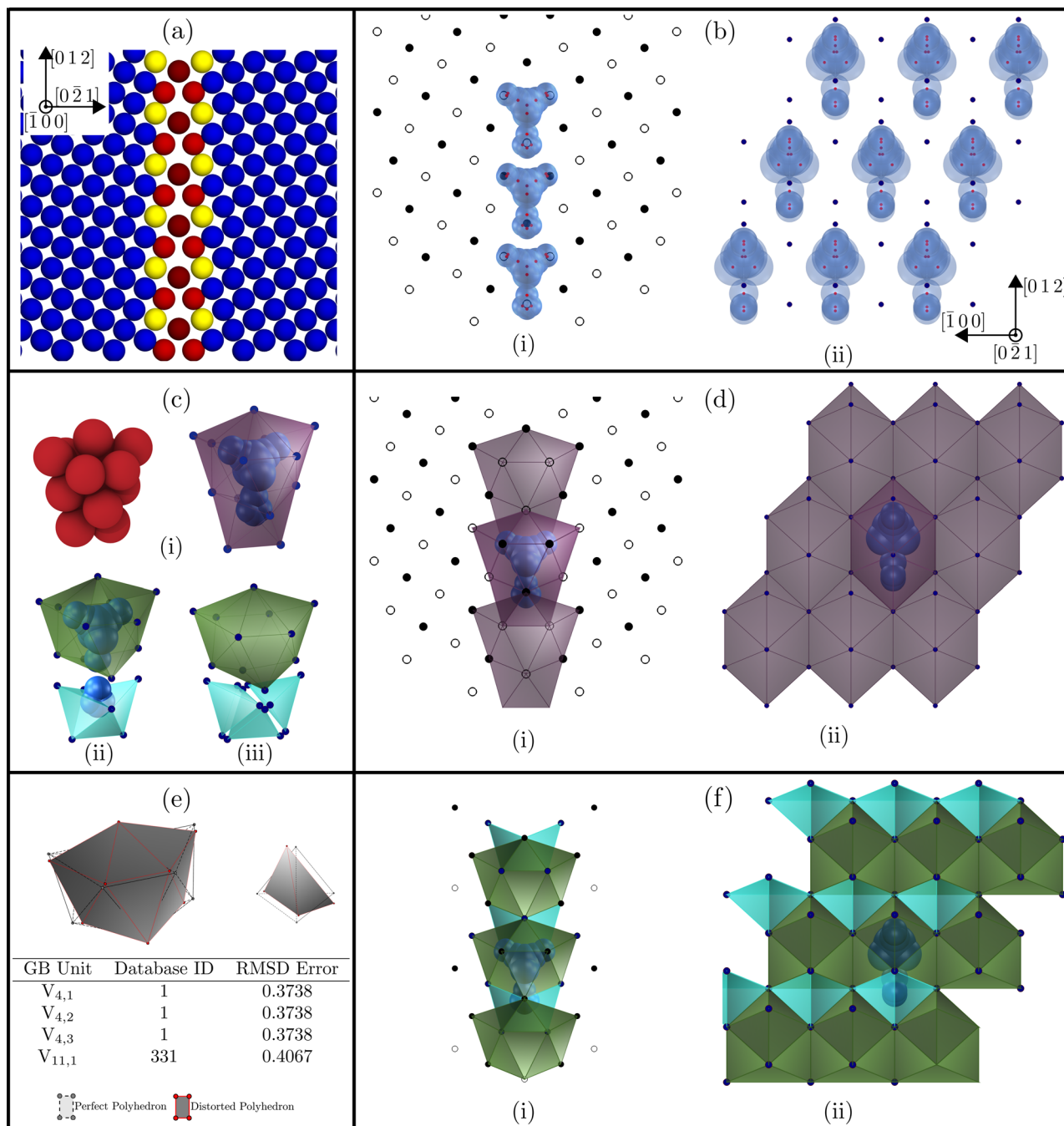


Fig. 2 An illustration of the VV-clustering algorithm for identifying the polyhedral unit structure of the $\Sigma 5(0\bar{2}1)$ GB. **a** The minimum energy atomistic structure (at 0 K) of the GB, generated using OVITO⁵⁹ is shown along the tilt axis $[\bar{1}00]$, where the atoms are colored according to their centro-symmetry parameter. **b**(i, ii) Atomistic structure of the GB along with the Voronoi vertices and VV-spheres are shown, as viewed along the tilt axis $[\bar{1}00]$ and the boundary-plane normal $[0\bar{2}1]$, respectively. All the Voronoi vertices of overlapping VV-spheres are clustered together and, in **c**(i) The polyhedral unit obtained by the clustering algorithm is shown. The polyhedron contains thirteen atoms. In **d**(i, ii), the polyhedral unit model of the $\Sigma 5(0\bar{2}1)$ along the tilt axis $[\bar{1}00]$ and the boundary-plane normal $[0\bar{2}1]$, respectively, are shown. Since the polyhedral unit is concave and contains more than 12 atoms, it is first split into smaller units by finding the interstitial voids of the 13-atom unit as shown in **c**(ii). The split units are then compared with the Cerfon-Holmes database and the iterative cluster (poly-tetrahedral unit) is split further into three tetrahedral units, as shown in **c**(iii). **e** The matching between the 11-atom and the best-match seed (octadecahedron) is shown. The registration between the highest-distorted tetrahedron and the perfect tetrahedron is also illustrated. The RMSD errors for all the resultant units in the GB are shown in the table. Finally, in **f**(i, ii), the structure of the GB, represented using the split units (octadecahedra and tetrahedra), is illustrated

the post-processing step takes advantage of the interstitial sites⁴² present in the larger concave units and splits them into polyhedra with less than 12 atoms.

Using these additional steps, the 13-atom unit observed in the $\Sigma 5(0\bar{2}1)$ GB is first split into smaller units containing 11 and 6 atoms each, as illustrated in Fig. 2c(ii). After splitting, the units are compared with the Holmes-Cerfon's database and the Root Mean-Square Distortion (RMSD) error (as described in section S3.1) is used to quantify the distortion between the observed GB unit and the perfect polyhedron in the database. The 6-atom unit is identified as an iterative poly-tetrahedral cluster that is split further into three tetrahedral units (as shown in Fig. 2c(iii)). The 11-atom unit is found to match with one of the seed clusters in the Holmes-Cerfon database (also known as the Octadecahedron) with an RMSD error of ~ 0.41 . The comparison between the GB polyhedral units and the seed units is shown in Fig. 2e along with the RMSD errors. In Fig. 2f (i, ii), the polyhedral unit structure of the $\Sigma 5(0\bar{2}1)$ GB is illustrated using split units, i.e., the octadecahedra and tetrahedra.

RESULTS

In this section, we present the 3D polyhedral unit model for GBs with increasing crystallographic complexity. We start with the analysis of two well-studied symmetric tilt GBs— $\Sigma 5(0\bar{1}3)(0\bar{1}\bar{3})$ and $\Sigma 11(1\bar{1}3)(1\bar{1}\bar{3})$, and a symmetric twist $\Sigma 49a(111)(\bar{1}\bar{1}\bar{1})$ GB. We then provide the polyhedral unit structures for a set of $\Sigma 3$ interfaces and conclude with the analysis of a general, mixed-character $\Sigma 49a(450, 221, 113)(\bar{9}\bar{2}\bar{5})$ GB. The computational details of the GB simulations are provided in the Methods section. The polyhedral unit structures of these GBs are described in the following paragraphs.

Symmetric Tilt and Twist Grain Boundaries

The structure of $\Sigma 5(0\bar{2}1)$, as shown in Fig. 2, contains 13-atom polyhedral units. A post-processing analysis results in the splitting of the 13-atom unit into an Octadecahedron and tetrahedral units.

Analysis of the polyhedral unit structure of $\Sigma 5(0\bar{1}3)$ GB shows that it contains an octadecahedron, a pentagonal bi-pyramid, and a dual-tetrahedron. The structure of this GB is shown along the tilt axis and along the normal to the GB in Fig. 3. The $\Sigma 5(0\bar{2}1)$ and the $\Sigma 5(0\bar{1}3)$ GBs are $[100]$ symmetric tilt GBs and are shown to contain the C-type and B-type structural units.⁴³ A comparison between the Octadecahedral units of the two GBs shows that they are very similar to each other; the RMSD error is ≈ 0.18 as shown in Fig. 3c(i). However, the primary difference between the two GBs is the placement of the Octadecahedral units, as illustrated in Fig. S28 of the Supplementary Information.

While the lowest-energy interfaces are physically significant, there exist meta-stable GB states, whose structure and properties also have an important role at high temperatures or if the material is processed under non-equilibrium conditions.⁴⁴ The VV-clustering algorithm described in this paper is applicable for the analysis of the metastable GB structures as well, and we provide a discussion of a meta-stable $\Sigma 5(0\bar{1}3)$ GB structure in section S4 of the Supplementary Information.

Another well-studied interface, using the structural unit model, is the $\Sigma 11(1\bar{1}3)$ GB, which is a symmetric tilt GB along the $[110]$ tilt axis. The polyhedral unit structure of this interface contains a stacking of capped-trigonal-prisms (CTPs) as shown in Fig. 4. From the perspective of a GB unit-cell, one CTP unit is sufficient to describe the complete structure of this GB. Such a GB may be defined as having a favored structure, a term coined by Sutton and Vitek.²⁵

The polyhedral unit analysis of the GB structure of a (111) symmetric twist GB, $\Sigma 49(111)$ is shown in Fig. 5a. The GB structure may also be described as a network of screw dislocations. The atoms that belong to the core of the dislocation are described through snub disphenoid units (Bernal canonical polyhedron with $n=8$ atoms). In Fig. 5b, the RMSD errors of the three unique snub-disphenoids observed in the twist GB are provided. The region where the dislocations intersect is described by a 14-atom polyhedral unit. In Fig. 5c, a canonical-model for this 14-atom unit, obtained through LAMMPS minimization, is shown.

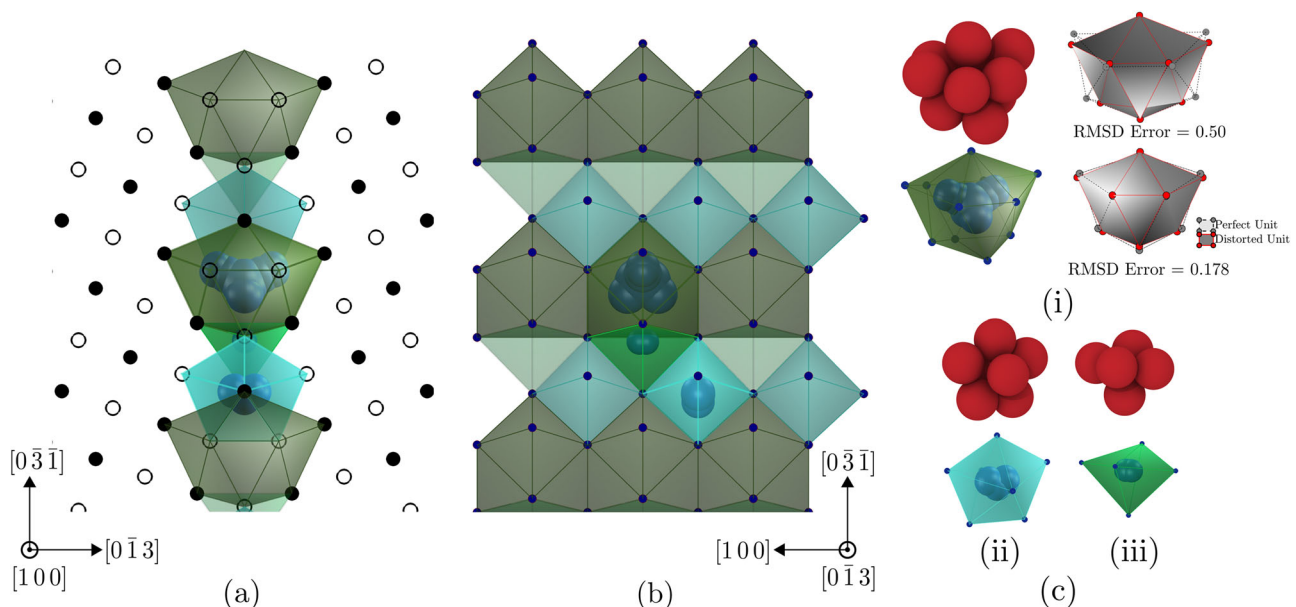


Fig. 3 The polyhedral unit model of the $\Sigma 5(0\bar{1}3)$ GB is illustrated. **a, b** The atomistic structure and the polyhedral units of the symmetric-tilt GB are shown, as viewed along the tilt axis $[100]$ and the plane normal $[0\bar{1}3]$, respectively. The polyhedral units corresponding to the smallest asymmetric unit (the unit-cell) are highlighted. **c** The unit-cell polyhedral units, which include (i) the Octadecahedron, (ii) the pentagonal bi-pyramid and (iii) the dual-tetrahedron along with the overlapping VV-spheres (Bernal holes) are illustrated. Also shown in **c**(i) is the comparison between the observed GB unit and the perfect Octadecahedron (RMSD error is equal to 0.5) and the $\Sigma 5(0\bar{2}1)$ Octadecahedron (RMSD error is approximately equal to 0.18)

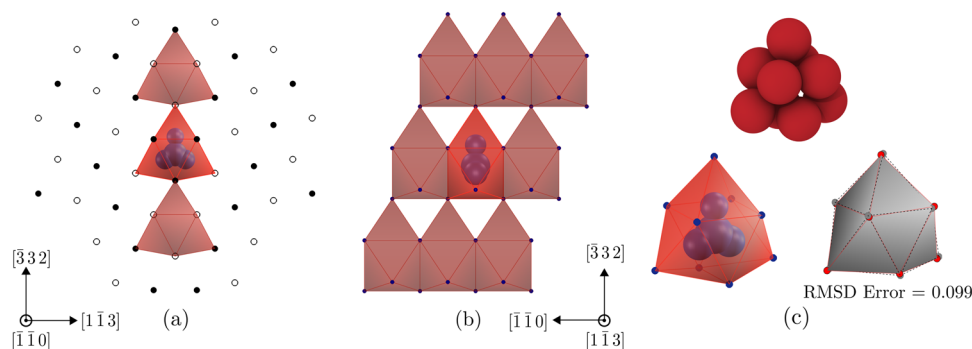


Fig. 4 The polyhedral unit model of the $\Sigma_{11}(\bar{1}\bar{1}3)$ GB is illustrated. **a, b** The atomistic structure and the polyhedral units (capped trigonal prisms) of the symmetric-tilt GB, along the tilt axis $[\bar{1}\bar{1}0]$ and the plane normal $[\bar{1}\bar{1}3]$, are shown. The CTP corresponding to the smallest asymmetric unit (the unit-cell) is highlighted. **c** The CTP and the overlapping VV-spheres (Bernal holes), along with the clusters of atoms that correspond to the CTP, are shown. Also illustrated is a comparison between the observed and a perfect CTP unit

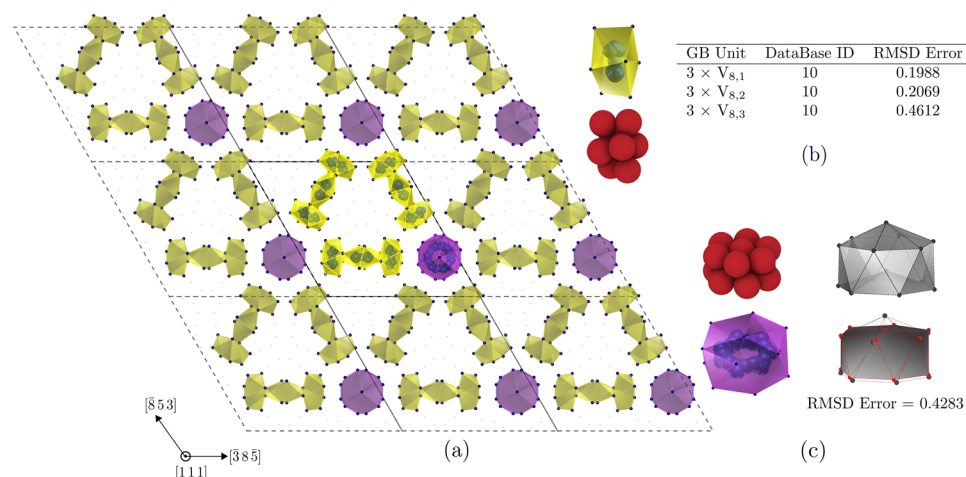


Fig. 5 The polyhedral unit model of the $\Sigma_{49}(111)$ GB, as viewed along the twist-axis $[111]$, is shown in **a**. The symmetric twist GB contains a network of screw dislocations. The core-region of the dislocation is described by the snub-disphenoid units and the atoms at the intersection of the screw dislocations are described by the 14-atom polyhedral unit. The smallest asymmetric unit (GB unit-cell) is shown and the polyhedral units in the unit-cell are highlighted. **b** The RMSD errors of the observed snub-disphenoids, when compared to the perfect unit, are shown. **c** The observed 14-atom polyhedral unit is minimized in LAMMPS and the relaxed structure is shown. Also shown are the two units superimposed on top of each other using the registration algorithm described in section S3.1. The planar primitive unit cell of the GB has been computed using the GBpy package (<https://pypi.python.org/pypi/GBpy>).⁶⁰

Grain Boundaries of Σ_3 Misorientation

In the following paragraphs, we provide a comparison of Σ_3 GB structures as the BPI orientation is varied. The set of Σ_3 GBs analyzed are shown in Fig. 6a using the Σ_3 BPI fundamental zone.²⁰ We start with the simplest of Σ_3 GBs, the $\Sigma_3(111)(\bar{1}\bar{1}1)$ interface, which may be characterized as a twist GB along the $[111]$ axis (the $\Sigma_3(111)$ GB is also classified as a symmetric tilt along $[0\bar{1}\bar{1}]$ axis or as the (111) twin GB). From an atomistic perspective, the twin GB could also be described as a stacking fault in the ABCABC... stacking sequence of an fcc crystal. The stacking fault results in a packing that is the same as the hcp single crystal stacking sequence. The polyhedral unit model of the twin GB consists of tetrahedra and octahedra (similar to the fcc single crystal). However, unlike the fcc crystal packing, the tetrahedra along the twin GB share a common face, and hence, correspond to dual-tetrahedra. The atoms that belong to the shared faces of the tetrahedra are positioned in the plane of the Σ_3 twin GB, as shown in Fig. 7. While the VV-spheres in the two tetrahedra that share a common face do not overlap, we present the structure of $\Sigma_3(111)$ GBs as a stacking of dual-tetrahedra in order to emphasize the difference between the polyhedral unit structure of the single crystal region and a stacking fault in the fcc lattice.

In Fig. 8, the structure of $\Sigma_3(2\bar{1}\bar{1})$ GB is illustrated, which contains CTPs and dual-tetrahedra. In this GB, octahedra that are distorted are also shown; we will use these distorted units to analyze the evolution of GB structure as the BPI orientation is varied. Also shown in Fig. 8c are the distortions in the observed GB units along with their RMSD errors. The structure of $\Sigma_3(10\bar{1})$ GB is shown in Fig. 9. This GB is an asymmetric tilt interface, with the tilt axis as $[1\bar{2}\bar{1}]$. In addition to the tetrahedra and octahedra, the GB contains a nine-atom polyhedral unit. The distortions of the polyhedral units observed in the $\Sigma_3(10\bar{1})$ GB, when compared to their canonical model units, are quantified in Fig. 9d.

We also present the structures of $\Sigma_3[01\bar{1}]$ asymmetric tilt GBs in Fig. 10. These were chosen as a comparison to the description of the structures of a same set of GBs analyzed by Tschopp and McDowell using the SU model.⁴⁵ According to the geometrical conventions defined in,⁴⁵ the inclination angle of the BPIs of $\Sigma_3(111)$, $\Sigma_3(11,5,5)$, $\Sigma_3(411)$, $\Sigma_3(100)$, $\Sigma_3(7\bar{2}\bar{2})$, $\Sigma_3(13,5,5)$, and $\Sigma_3(2\bar{1}\bar{1})$ GBs correspond to $\theta = 0^\circ, 22.0^\circ, 35.26^\circ, 54.74^\circ, 76.74^\circ, 83.28^\circ$, and 90° , respectively. The positions of these GBs are also shown in the BPI fundamental zone of the Σ_3 misorientation (Fig. 6a). With respect to the fundamental zone, the inclination of all possible Σ_3 GBs may be specified using their polar coordinates

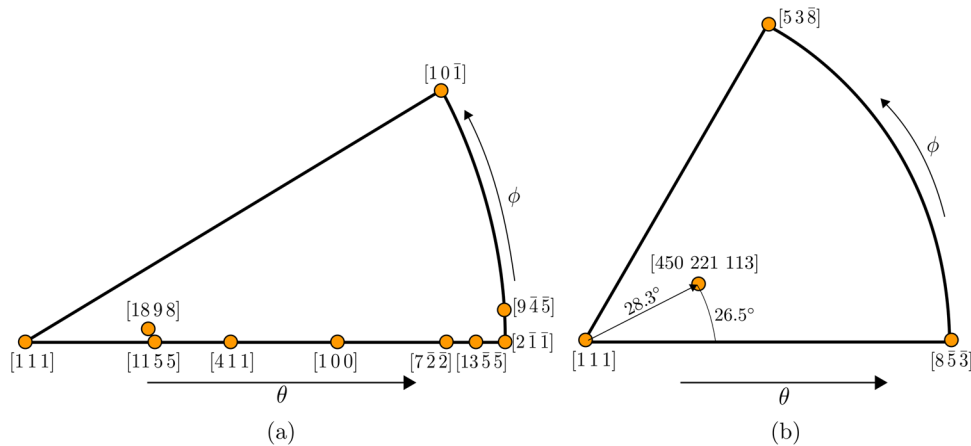


Fig. 6 The boundary-plane fundamental zones of **a** $\Sigma 3$ and **b** $\Sigma 49a$ misorientations are illustrated. The GBs analyzed in this article are highlighted and the indices of the boundary-plane normal vectors are provided

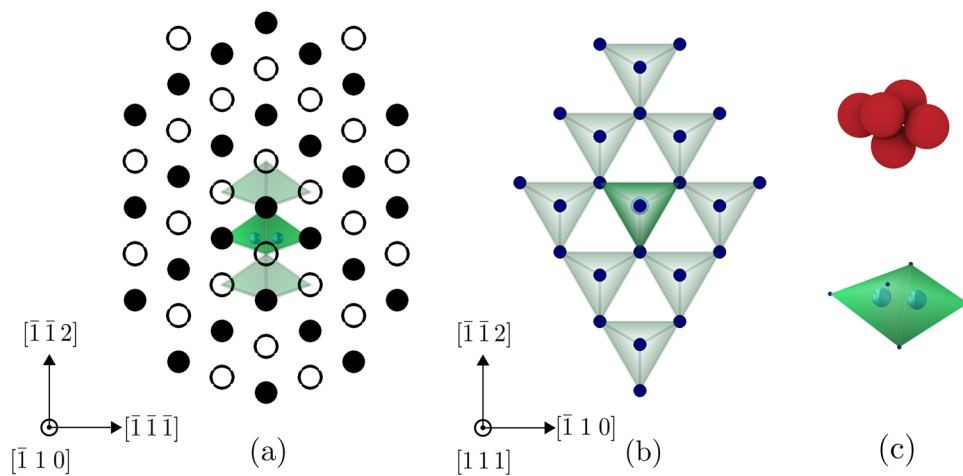


Fig. 7 The polyhedral unit model of the $\Sigma 3(111)$ GB is illustrated. **a, b** The atomistic structure and the dual-tetrahedral units of the twin GB, viewed along the tilt axis $[\bar{1}10]$ and along the plane normal $[111]$, respectively, are shown. Due to the translational symmetry of the GB, the unit-cell contains only one dual-tetrahedron, which is highlighted. **c** The dual-tetrahedron along with the corresponding atoms and the VV-spheres are shown. As discussed in the article, the VV-spheres of the dual-tetrahedron in the twin GB do not overlap

(θ, ϕ) . The $\Sigma 3(111)$ GB has the orientation $(\theta, \phi) = (0, 0)$, and $\Sigma 3(2\bar{1}\bar{1})$ corresponds to $(90^\circ, 0)$. The asymmetric tilt $\Sigma 3[01\bar{1}]$ GBs correspond to set of orientations with $\phi = 0$.

A faceting model, containing the structural units D ($\Sigma(111)$) and DC ($\Sigma 3(2\bar{1}\bar{1})$), has been proposed for these asymmetric tilt GBs.⁴⁵ The polyhedral unit models of all the seven GBs, as viewed along the tilt axis, are shown in Fig. 10 and the faceting model is clearly apparent for these asymmetric tilts. The fundamental polyhedral unit of the $\Sigma 3(111)$ GB is the dual-tetrahedron and the $\Sigma 3(2\bar{1}\bar{1})$ GB contains CTPs, dual-tetrahedra and distorted-octahedra. The dual-tetrahedra of the $\Sigma 3(2\bar{1}\bar{1})$ GB are not shown in this figure for easier interpretation of the faceting model (the orientation of the dual-tetrahedra present in the $\Sigma 3(2\bar{1}\bar{1})$ GB is different from that of the $\Sigma 3(111)$ GB). The twin-facets are present in $\Sigma 3(111)$, $\Sigma 3(11,5,5)$, and $\Sigma 3(411)$ GBs. The last four GBs do not contain the $\Sigma 3(111)$ twin facet and only contain units that correspond to the $\Sigma 3(2\bar{1}\bar{1})$ GB. The difference in the BPI orientation is accommodated by changing the position of the CTP units with respect to the octahedral units in the GB. A discussion of the sliding of polyhedral units, to accommodate the variation in BPI orientation, is provided in section S6 of the [Supplementary Information](#). Finally, in Fig. 10h, we present an analysis of the distortion of the CTP unit as the tilt angle θ varies from 90° (corresponding to $\Sigma 3(2\bar{1}\bar{1})$ GB in Fig. 10g) to 22° (corresponding to $\Sigma 3(11,5,5)$ GB in

Fig. 10b). The CTP unit in the $\Sigma 3(2\bar{1}\bar{1})$ GB is used as the reference structure and the registration algorithm described in section S3.1 of the [Supplementary Information](#) is utilized to compute the RMSD errors. As shown, the distortion gradually increases and plateaus around 0.075 as the BPI orientation is varied. The polyhedral unit model, therefore, not only provides a basis for analyzing GB structures, but when used in conjunction with the registration algorithm, provides a powerful tool for the quantitative comparison of GBs across the crystallographic phase-space.

In Fig. 11, we show the structure of $\Sigma 3(9\bar{4}\bar{5})$, which is an asymmetric tilt GB (along the $[111]$ tilt axis). The BPI orientation of this GB, as is evident from Fig. 6a, is vicinal to the $\Sigma 3(2\bar{1}\bar{1})$ symmetric tilt GB. The orientation of $\Sigma 3(9\bar{4}\bar{5})$ GB in the polar coordinates is $(\theta, \phi) = (90^\circ, 3.76^\circ)$. Therefore, the structure of this GB contains primarily of units corresponding to the singular $\Sigma 3(2\bar{1}\bar{1})$ GB with a ledge.⁴⁶ The structure of the ledge is more complex with two polyhedral units of 15 and 11 atoms each, as shown in Fig. 11d. The blue polyhedral unit, which contains 15 atoms, has features similar to the CTP unit and the orange polyhedral unit, which contains 11 atoms, is an extension of the distorted octahedral units presented in Fig. 8. These polyhedral units have been identified automatically through the VV-clustering algorithm. It is anticipated that, GB defects, such as ledges, steps and kinks will contain irregular units with a larger number of atoms in the

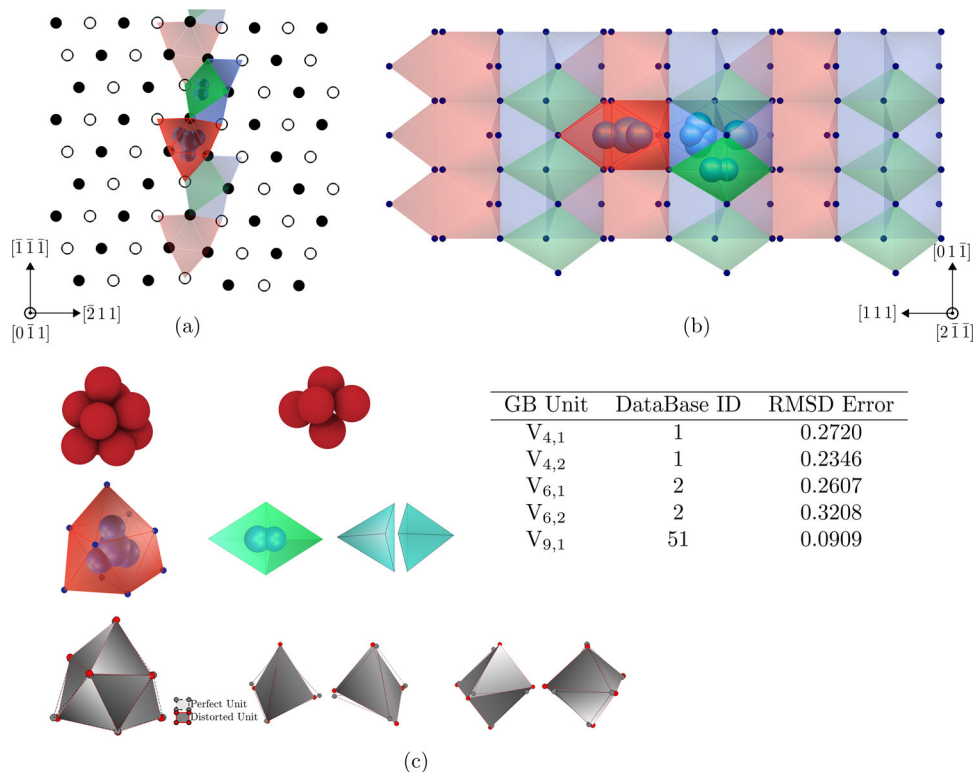


Fig. 8 The polyhedral unit model of the $\Sigma 3(2\bar{1}\bar{1})$ GB is illustrated. **a, b** The atomistic structure and the polyhedral units (CTPs, dual-tetrahedra and distorted octahedra) of the symmetric-tilt GB, along the tilt axis $[0\bar{1}\bar{1}]$ and the plane normal $[2\bar{1}\bar{1}]$, are shown. The polyhedral units corresponding to the smallest asymmetric unit (the unit-cell) are highlighted. The registration of the five unique polyhedral units with their corresponding model units is illustrated in **c**. The model units for the 9, 6 and 4-atom units are the capped-trigonal-prism, octahedron and the tetrahedron, respectively. In the table, these model units are identified according to their “IDs” in the data-base. The RMSD errors for these units are also provided

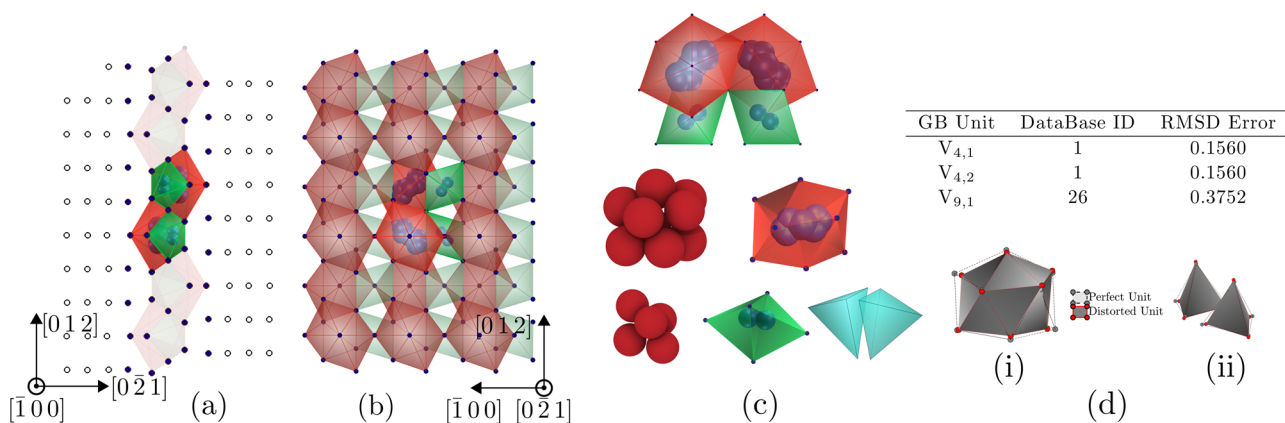


Fig. 9 The polyhedral unit model of the $\Sigma 3(10\bar{1})$ asymmetric tilt GB is illustrated. **a, b** The atomistic structure and the polyhedral units, along the tilt axis $[1\bar{2}\bar{1}]$ and the plane normal $[10\bar{1}]$, are shown. The polyhedral units corresponding to the smallest asymmetric unit (the unit-cell) are highlighted. **c** The unit-cell polyhedral units, along with the overlapping VV-spheres (Bernal holes) and the clusters of atoms that correspond to the polyhedral units, are shown. The unique GB overlaps are the 9-atom unit and the 5-atom dual-tetrahedron. The dual-tetrahedron is split further into two seed tetrahedra. The 9-atom GB unit best fits a 9-atom seed cluster in the data-base with RMSD error of ~ 0.38

identified polyhedra. The classification of these units is described in section S3.3.2 of the [Supplementary Information](#).

In Fig. 12, we present the structure of $\Sigma 3(18,9,8)$ GB, which is an interface with mixed character. The polar coordinates of the GB are $(\theta, \phi) = (21.1^\circ, 5.21^\circ)$ and the position of the GB in the $\Sigma 3$ BPI fundamental zone is shown in Fig. 6a. While the GB has both twist and tilt components, it has large facets corresponding to the $\Sigma 3(111)$ GB due to its proximity to the twin GB (as shown in Fig. 6a).

The rest of the structure primarily consists of the CTPs, which is a signature of the $\Sigma 3(2\bar{1}\bar{1})$ GB. The $\Sigma 3(18,9,8)$ contains the fifteen-atom polyhedral unit that corresponds to the ledge observed in $\Sigma 3(9\bar{4}\bar{5})$. Additionally, $\Sigma 3(18,9,8)$ also contains an infinite cluster of atoms (shown as orange units). This unit represents regions that have higher excess-volume as the Voronoi spheres overlap with each other along a large region in the GB. Figure 12c shows the side view of the infinite unit, which has the exact same

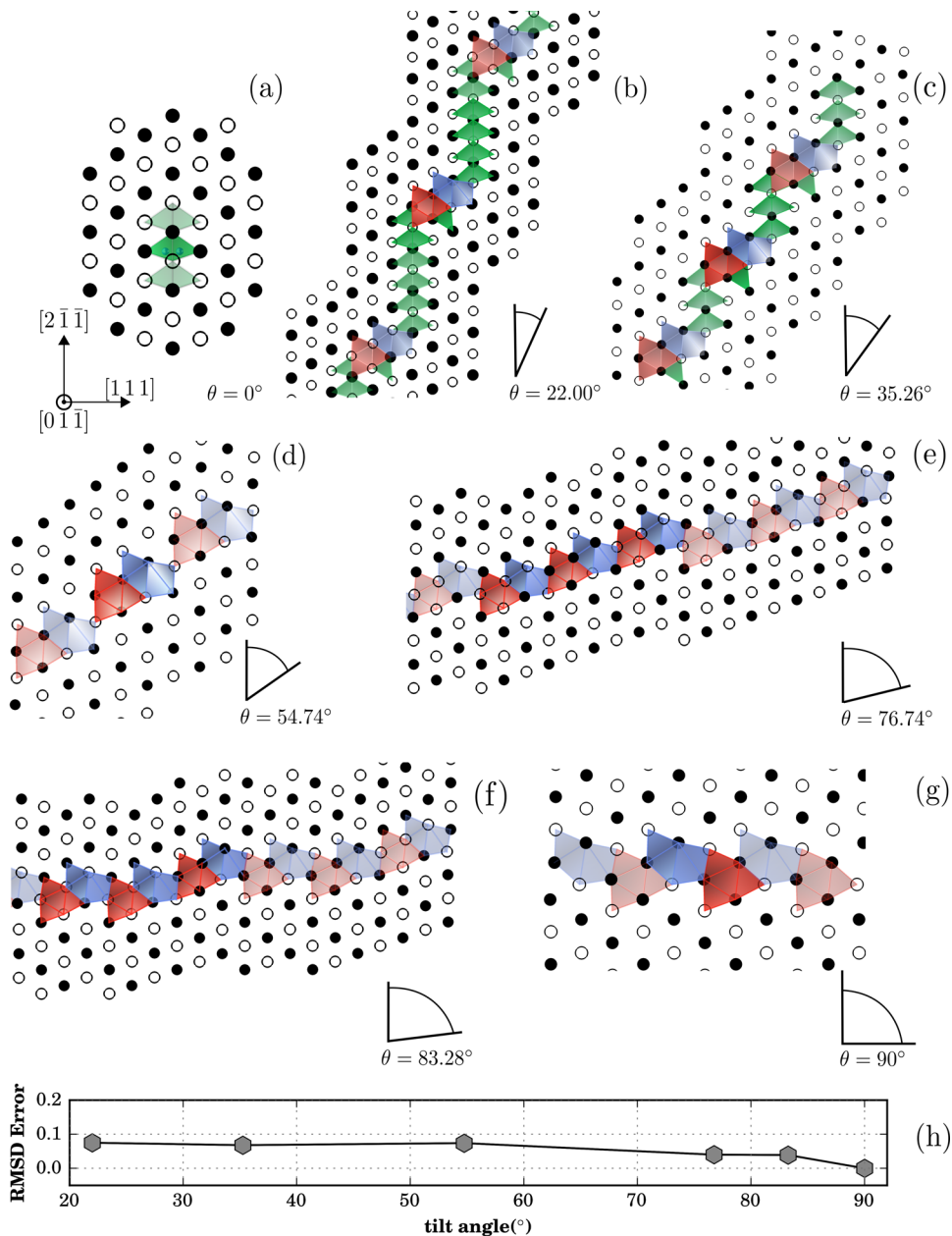


Fig. 10 The polyhedral unit structures of the $\Sigma 3$ asymmetric tilt GBs, along the $[0\ 1\ \bar{1}]$ tilt axis, are shown. The order of the GBs are as follows: **a** $\Sigma 3(111)$, **b** $\Sigma 3(11,5,5)$, **c** $\Sigma 3(411)$, **d** $\Sigma 3(100)$, **e** $\Sigma 3(7\ 2\ 2)$, **f** $\Sigma 3(13, 5, 5)$, and **g** $\Sigma 3(2\ \bar{1}\ \bar{1})$. The faceting model is apparent in the GBs shown in **b** and **c**, which contain polyhedral units of both the $\Sigma 3(111)$ and $\Sigma 3(2\ \bar{1}\ \bar{1})$ GBs. **d–f** While there are no twin facets, deviations in boundary-plane orientations are accommodated by sliding the CTP units over the distorted octahedra. An example of this is shown in Figure S29 of the [Supplementary Information](#). **h** The distortion of the CTP units, when compared to a similar unit in the $\Sigma 3(2\ \bar{1}\ \bar{1})$ GB, is quantified and plotted against the tilt angle θ

arrangement as the distorted octahedra (the blue octahedral units in Fig. 8a) in $\Sigma 3(2\ \bar{1}\ \bar{1})$ GB. This arrangement of distorted octahedra naturally arises when the post-processing steps are applied to the infinite cluster. The details of this analysis are presented in section S3.3.3 of the [Supplementary Information](#).

These observations suggest that the $\Sigma 3(18,9,8)$ GB contains polyhedral units that are present in the $\Sigma 3(111)$ and $\Sigma 3(2\ \bar{1}\ \bar{1})$ GBs, which supports a 3D faceting-type model. The faceting of $\Sigma 3$ GBs has been hypothesized using the Wulff construction on the $\Sigma 3$ GB energy landscape measured both experimentally⁴⁷ and through atomistic simulations.²⁰ It is observed that the polyhedra that correspond to the intersections of the facets, which are termed as steps or ledges, have a similar geometry in the $\Sigma 3$ misorientation

space. For example, the fifteen atom unit is similar to the cluster of atoms observed in $\Sigma 3(9\ 4\ 5)$ and hence accommodates the perturbation in the angle ϕ of the BPI orientation.

Mixed character $\Sigma 49a$ boundary

While the $\Sigma 3(18,9,8)$ GB is neither a tilt nor a twist GB, it is still vicinal (by $\sim 5.21^\circ$) to the set of $\Sigma 3$ asymmetric tilt GBs. In order to demonstrate the utility of the VV-clustering algorithm, we present the polyhedral unit structure of a more general GB, $\Sigma 49a(4\ 5\ 0, 2\ 2\ 1, 1\ 1\ 3)(\bar{9}\ \bar{2}\ \bar{5})$ in aluminum (this GB will be referred to as $\Sigma 49a(925)$ in the following discussion). This high- Σ misorientation corresponds to a rotation angle of approximately

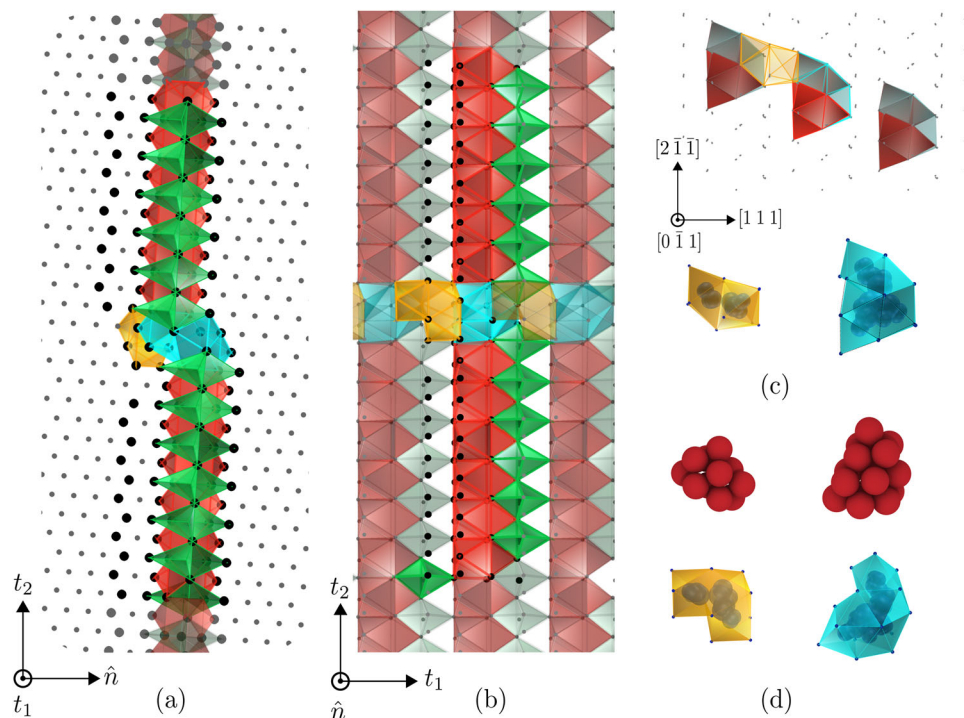


Fig. 11 The polyhedral unit model of the $\Sigma 3(9\bar{4}5)$ asymmetric tilt GB is illustrated. **a, b** The atomistic structure along with the polyhedral units are shown. The vector $\vec{t}_1 = [111]$ is the tilt axis, $\hat{n} = [9\bar{4}5]$ is the BPI normal and $\vec{t}_2 = [\bar{1}, 14, \bar{1}3]$. This GB is vicinal to the $\Sigma 3(2\bar{1}\bar{1})$ symmetric tilt GB. Therefore, it contains facets of the CTP units and two polyhedral units (colored in blue and orange) that are a part of the ledge in the vicinal GB. **c** The same GB is shown along the $[0\bar{1}1]$ axis, without the dual-tetrahedral units, to emphasize the polyhedral units along the ledge. **d** The polyhedral units that belong to the ledge and the clusters of atoms that correspond to these units are shown

43.58° degrees along the $[111]$ axis. The BPI orientation is also not vicinal to any of the symmetric or asymmetric tilts as shown in the BPI fundamental zone of the $\Sigma 49a$ misorientation in Fig. 6b. As a result of the reasonably large Σ number and the mixed character of the interface, it is anticipated that the atomic structure of this interface is highly disordered. In Fig. 13, the polyhedral unit representation, computed using the VV-clustering algorithm and the post-processing analysis, of the zero-Kelvin lowest energy structure of $\Sigma 49a(925)$ GB in aluminum is shown.

Listed in Table S3 in Supplementary Information, are the number of polyhedral units, classified according to the number of vertices (or atoms), and their frequency of occurrence in the $\Sigma 49a(925)$ GB. A complete classification of the different types of polyhedral units that may be observed in this general GB is provided in section S3.4 of the Supplementary Information. For example, most of the observed polyhedra, with greater than seven atoms, may be classified as (i) snub disphenoids for $n=8$ (68 units), (ii) capped-trigonal prisms for $n=9$ (48 units), (iii) ID = 1 unit in the data-base with 10 atoms (24 out of 32), (iv) ID = 432 unit with 11 atoms (12 out of 21) and (v) ID = 6730 unit with 12 atoms (4 out of 5). We have also analyzed the polyhedral unit structure of the $\Sigma 49a(853)$ interface, which is a $[111]$ symmetric tilt GB (Fig. S23). The polyhedral units found in this symmetric tilt GB include two capped-trigonal prisms, one 11-atom unit (ID = 432), and two 12-atom units (IDs = 6730 and 821). The presence of common geometrical motifs among these two interfaces (capped-trigonal prisms for $n=9$, ID = 432 for $n=11$, and ID = 6730 for $n=12$) supports a strong correlation between GB structure and crystallographic parameters. The polyhedral unit model provides a unique tool that facilitates the comparison of GB structures in the five-dimensional crystallographic phase-space (i.e., both the misorientation and the boundary-plane orientations). Finally, it is emphasized that a statistical analysis of the different GB

polyhedral units is anticipated to provide a fundamental set of geometrical motifs that may be observed in metallic interfaces.

DISCUSSION

The polyhedral unit model described in this article provides a coarse-grained geometric description of structure and atomic packing in grain boundaries. This model is expected to replace the traditional structural unit model and provides a tool for comparing GBs that are crystallographically similar in the five-parameter space. For example, in this article, we have demonstrated the utility of the polyhedral unit model by comparing GB structures with a fixed misorientation ($\Sigma 3$ and $\Sigma 49a$) and varying boundary-plane orientations.

The polyhedral structure of a GB is computed through an automated algorithm that involves two steps: (i) the clustering of vertices of the Voronoi polyhedra in the GB structure and (ii) a comparison of the observed units with a database of rigid hard-sphere packings using the registration algorithm. The post-processing analyses along with the metric quantifying the distortions allows for a robust classification of the observed GB polyhedral units. In particular, the metric proposed in section S3.1 will further enable the application of unsupervised learning algorithms,⁴⁸ such as clustering analysis in the space of observed GB polyhedral units. Such learning algorithms can be utilized to obtain a fundamental set of polyhedral units that will exist in GB structures.

The polyhedral unit model also classifies the void structure (or the Bernal holes) in the GB. It is anticipated that the classification of the void structure may be utilized to predict segregation sites of small solute atoms where the energetics are dominated by the volume of the interstitial sites rather than the interaction between the metal atoms and the solute segregant. For example, in Fig. S30, we show an excellent agreement between the oxygen

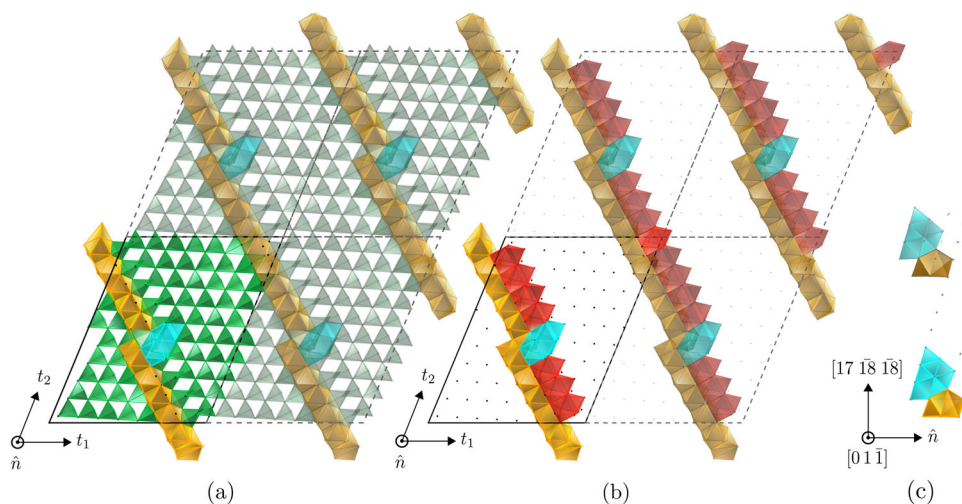


Fig. 12 The polyhedral unit model of the $\Sigma 3(18,9,8)$ general GB is illustrated. **a, b** The atomistic structure along with the polyhedral units are shown. Two images along the same view (i.e., along the boundary-plane normal vector, $\hat{n} = [18, 9, 8]$) are provided to simplify the presentation. The long orange units are repeated in the two views. The vectors \vec{t}_1 and \vec{t}_2 are along $[5\bar{2}9]$ and $[1\bar{2}0]$, respectively. This GB is close in orientation to the $\Sigma 3(111)$ GB, and hence, contains twin facets (represented by the green dual-tetrahedral units). The GB also has the CTP units that correspond to the polyhedral units of the $\Sigma 3[2\bar{1}\bar{1}]$ GB. The two-dimensional unit cells of the GBs are highlighted and four unit cells are shown. The GB contains ledges and the polyhedral units that belong to these ledges are the same as those observed in the $\Sigma 3(9\bar{4}5)$. The blue polyhedral unit has the same structure as shown in Fig. 11 with fifteen atoms. The long polyhedral unit (shown in orange) is an extension of the orange polyhedral unit shown in Fig. 11. The polyhedral units of the ledge are emphasized in **c** by viewing the GB along the $[01\bar{1}]$ axis

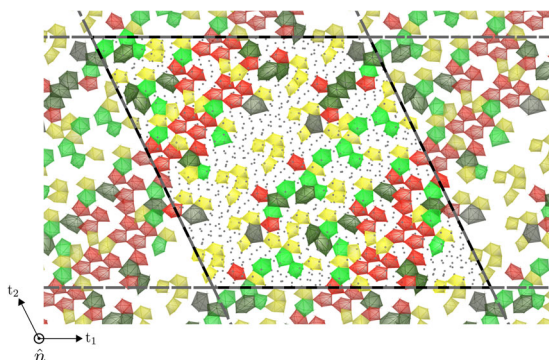


Fig. 13 The polyhedral unit model of the $\Sigma 49a(450, 221, 113)(\bar{9}\bar{2}\bar{5})$ general GB is illustrated. The units shown here are those obtained after the post-processing analysis described in section S3.4 of the [Supplementary Information](#). The unit-cell of the GB is described by vectors $\vec{t}_1 = [5, 2, 16]$ and $\vec{t}_2 = [\bar{1}6, 29, 7]$. The boundary-normal vector along which the GB is viewed in this figure is $\hat{n} = [450, 221, 113]$. The two-dimensional unit cells of the GB are highlighted. For the sake of simplicity, only units with greater than seven atoms are shown in this figure

segregation sites (obtained through DFT computations)⁴⁹ and the voids in the polyhedral units for $\Sigma 5(0\bar{2}1)$ and $\Sigma 11(1\bar{1}3)$ GBs. The void structure of the GBs is also anticipated to play an important role in analyzing the diffusivity of small interstitial solute atoms along the GBs. For example, the infinitely long polyhedral unit in the structure of $\Sigma 3(18,9,8)$, which has a similar atomic packing as found in the E structural unit observed in $[110]$ symmetric tilt GBs,^{50, 51} may provide a fast diffusion-path along this interface, or enable shuffling events during GB sliding.⁵² These long units correspond to extended regions of overlapping Voronoi-spheres (or regions of excess volume) in the disordered region of the GB.

The polyhedral unit model also provides a link between the analysis of GB structures and those observed in metallic glasses, thus paving a way towards analyzing GB dynamics through the structural theories proposed for glassy systems.^{53, 54} For example,

GB excess volume is an important geometric parameter, which is purported to influence a wide-array of GB properties.^{51, 55–58} The polyhedral unit model provides a valuable tool for visualizing the spatial correlations of excess volume along the interface. Finally, while the examples provided in this article are of aluminum GBs, it is anticipated that this technique is applicable for the analysis of interfaces in mono-atomic metallic systems. In particular, an intuitive polyhedral-unit structure is expected to be valuable for grain boundaries in close-packed systems, such as hexagonal lattices.

METHODS

The GB structures analyzed in this article correspond to the lowest-energy structures obtained at zero-Kelvin for aluminum. These structures are obtained through standard simulation techniques developed for generating GB structures and complete details of the simulation methodology are provided in ref. 20. Mishin's EAM potential⁴¹ is utilized for simulating aluminum GBs. This force-field has been validated for its ability to predict the surface energies for aluminum by comparing the energies computed from MD simulations to those obtained through ab initio simulations. Additionally, the potential has been optimized to reproduce the stable and un-stable stacking fault energies accurately in aluminum. Since the stacking fault energies and the width of the dislocation disassociation are crucial parameters in GB simulations, it is expected that Mishin's EAM potential will reproduce experimentally observed GB structures.

ACKNOWLEDGEMENTS

We acknowledge Prof. Julian McAuley from University of California, San Diego, for sharing the two-dimensional point-pattern matching code. The computational support was provided by the High Performance Computing Center at North Carolina State University. This work was supported by start-up funds from North Carolina State University and by NSF CAREER award DMR#1554270.

AUTHOR CONTRIBUTIONS

A.D.B. and S.P. designed the project; A.D.B. performed all the simulations and developed all the analysis codes. All authors contributed to discussion of the results and preparation of the manuscript.

COMPETING INTERESTS

The authors declare no competing interests.

REFERENCES

- Patala, S., Mason, J. K. & Schuh, C. A. Improved representations of misorientation information for grain boundary science and engineering. *Prog. Mater. Sci.* **57**, 1383–1425 (2012).
- Mishin, Y. & Herzig, C. Grain boundary diffusion: recent progress and future research. *Mater. Sci. Eng. A* **260**, 55–71 (1999).
- Chen, Y. & Schuh, C. A. Diffusion on grain boundary networks: percolation theory and effective medium approximations. *Acta Mater.* **54**, 4709–4720 (2006).
- Deng, J., Morgan, D. & Szuflarska, I. Kinetic monte carlo simulation of the effective diffusivity in grain boundary networks. *Comput. Mater. Sci.* **93**, 36–45 (2014).
- Mondal, P., Klein, A., Jaegermann, W. & Hahn, H. Enhanced specific grain boundary conductivity in nanocrystalline Y_2O_3 —stabilized zirconia. *Solid State Ionics*. **118**, 331–339 (1999).
- Babcock, S. & Vargas, J. The nature of grain boundaries in the high-*tc* superconductors. *Ann. Rev. Mater. Sci.* **25**, 193–222 (1995).
- Frary, M. & Schuh, C. Nonrandom percolation behavior of grain boundary networks in high-*tc* superconductors. *Appl. Phys. Lett.* **83**, 3755–3757 (2003).
- Cheung, C., Erb, U. & Palumbo, G. Application of grain boundary engineering concepts to alleviate intergranular cracking in alloys 600 and 690. *Mater. Sci. Eng. A* **185**, 39–43 (1994).
- Kokawa, H. Weld decay-resistant austenitic stainless steel by grain boundary engineering. *J. Mater. Sci.* **40**, 927–932 (2005).
- Gupta, G. *et al.* Role of grain boundary engineering in the scc behavior of ferritic–martensitic alloy ht-9. *J. Nucl. Mater.* **361**, 160–173 (2007).
- Krupp, U., Wagenhuber, P.-G., Kane, W. & McMahon, C. Improving resistance to dynamic embrittlement and intergranular oxidation of nickel based superalloys by grain boundary engineering type processing. *Mater. Sci. Technol.* **21**, 1247–1254 (2005).
- Bechtle, S., Kumar, M., Somerday, B. P., Launey, M. E. & Ritchie, R. O. Grain-boundary engineering markedly reduces susceptibility to intergranular hydrogen embrittlement in metallic materials. *Acta Mater.* **57**, 4148–4157 (2009).
- Homer, E. R., Patala, S. & Priedeman, J. L. Grain boundary plane orientation fundamental zones and structure–property relationships. *Sci. Rep.* **5**, 15476 (2015).
- Johnson, O. K., Li, L., Demkowicz, M. J. & Schuh, C. A. Inferring grain boundary structure–property relations from effective property measurements. *J. Mater. Sci.* **50**, 6907–6919 (2015).
- Rohrer, G. S. Grain boundary energy anisotropy: a review. *J. Mater. Sci.* **46**, 5881–5895 (2011).
- Stukowski, A., Bulatov, V. V. & Arsenlis, A. Automated identification and indexing of dislocations in crystal interfaces. *Model. Simul. Mater. Sci. Eng.* **20**, 085007 (2012).
- Stukowski, A. Structure identification methods for atomistic simulations of crystalline materials. *Model. Simul. Mater. Sci. Eng.* **20**, 045021 (2012).
- Patala, S. & Schuh, C. A. Symmetries in the representation of grain boundary-plane distributions. *Philos. Mag.* **93**, 524–573 (2013).
- Balluffi, R. & Sutton, A. in *Materials Science Forum*, Vol. 207, 1–12 (Trans Tech Publ, 1996).
- Banadaki, A. D. & Patala, S. A simple faceting model for the interfacial and cleavage energies of $\Sigma 3$ grain boundaries in the complete boundary plane orientation space. *Comput. Mater. Sci.* **112**, 147–160 (2016).
- Rosenhain, W. & Ewen, D. Intercrystalline cohesion in metals. *J. Inst. Metals* **8**, 149–185 (1912).
- Hargreaves, F. & Hills, R. Work-softening and a theory of intercrystalline cohesion. *J. Inst. Metals* **41**, 257–283 (1929).
- Bishop, G. H. & Chalmers, B. A coincidence-ledge-dislocation description of grain boundaries. *Scr. Metal.* **2**, 133–139 (1968).
- Sutton, A. & Vitek, V. On the structure of tilt grain boundaries in cubic metals I. symmetrical tilt boundaries. *Philos. Trans. R. Soc. Lond. A Math. Phys. Sci.* **309**, 1–36 (1983).
- Sutton, A. & Vitek, V. On the structure of tilt grain boundaries in cubic metals II. asymmetrical tilt boundaries. *Philos. Trans. R. Soc. Lond. A Math. Phys. Sci.* **309**, 37–54 (1983).
- Rittner, J. & Seidman, D. N. in *Materials Science Forum*, Vol. 207, 333–336 (Trans Tech Publ, 1996).
- Ashby, M., Spaepen, F. & Williams, S. The structure of grain boundaries described as a packing of polyhedra. *Acta Metall.* **26**, 1647–1663 (1978).
- Bernal, J. D. A geometrical approach to the structure of liquids. *Nature*. **183**, 141–147 (1959).
- Bernal, J. D. & Finney, J. L. Random close-packed hard-sphere model. II. geometry of random packing of hard spheres. *Discuss. Faraday Soc.* **43**, 62–69 (1967).
- Yamamoto, R., Haga, K., Shibuta, H. & Doyama, M. Search for bernal holes in a realistic structural model of amorphous iron. *J. Phys. F: Metal Phys.* **8**, L179–L182 (1978).
- Frost, H., Ashby, M. & Spaepen, F. A first report on a systematic study of tilt-boundaries in hard-sphere fcc crystals. *Scr. Metal.* **14**, 1051–1056 (1980).
- Frost, H. J., Spaepen, F. & Ashby, M. F. A second report on tilt boundaries in hard sphere fcc crystals. *Scr. Metal.* **16**, 1165–1170 (1982).
- Frost, H., Ashby, M. & Spaepen, F. A. A Catalogue of [100],[110], and [111]. *Symmetric Tilt Boundaries in Face-Centered Cubic Hard Sphere Crystals*. Materials Research Laboratory Technical Report (National Science Foundation Grant DMR 80-20247, 1982).
- Briant, C. & Messmer, R. An electronic model for the effect of alloying elements on the phosphorus induced grain boundary embrittlement of steel. *Acta Metall.* **30**, 1811–1818 (1982).
- Zhou, X., Marchand, D., McDowell, D. L., Zhu, T. & Song, J. Chemomechanical origin of hydrogen trapping at grain boundaries in fcc metals. *Phys. Rev. Lett.* **116**, 075502 (2016).
- Holmes-Cerfon, M. C. Enumerating rigid sphere packings. *SIAM Rev.* **58**, 229–244 (2016).
- Flores, K. *et al.* Characterization of free volume in a bulk metallic glass using positron annihilation spectroscopy. *J. Mater. Res.* **17**, 1153–1161 (2002).
- Slipenyuk, A. & Eckert, J. Correlation between enthalpy change and free volume reduction during structural relaxation of $Zr_{55}Cu_{30}Al_{10}Ni_5$ metallic glass. *Scr. Mater.* **50**, 39–44 (2004).
- Starr, F. W., Sastry, S., Douglas, J. F. & Glotzer, S. C. What do we learn from the local geometry of glass-forming liquids? *Phys. Rev. Lett.* **89**, 125501 (2002).
- Plimpton, S. Fast parallel algorithms for short-range molecular dynamics. *J. Comput. Phys.* **117**, 1–19 (1995).
- Mishin, Y., Farkas, D., Mehl, M. & Papaconstantopoulos, D. Interatomic potentials for monoatomic metals from experimental data and ab initio calculations. *Phys. Rev. B* **59**, 3393 (1999).
- Frost, H. Cavities in dense random packings. *Acta Metall.* **30**, 889–904 (1982).
- Frost, H. M. A., Spearot, D. E. & McDowell, D. L. Influence of grain boundary structure on dislocation nucleation in fcc metals. *Disloc. Solids* **14**, 43–139 (2008).
- Han, J., Vitek, V. & Srolovitz, D. J. Grain-boundary metastability and its statistical properties. *Acta Mater.* **104**, 259–273 (2016).
- Tschopp, M. & McDowell, D. Structures and energies of $\Sigma 3$ asymmetric tilt grain boundaries in copper and aluminium. *Philos. Mag.* **87**, 3147–3173 (2007).
- Sutton, A. P. & Balluffi, R. W. *Interfaces in Crystalline Materials* (Clarendon Press, 1995).
- Kucherinenko, Y., Protasova, S. G. & Straumal, B. B. in *Defect and Diffusion Forum*, Vol. 237, 584–592 (Trans Tech Publ, 2005).
- Hastie, T., Tibshirani, R. & Friedman, J. in *The Elements of Statistical Learning*, 485–585 (Springer, 2009).
- Chen, J. & Dongare, A. M. Role of grain boundary character on oxygen and hydrogen segregation-induced embrittlement in polycrystalline Ni. *J. Mater. Sci.* **52**, 30–45 (2017).
- Tschopp, M., Tucker, G. & McDowell, D. Structure and free volume of $\langle 110 \rangle$ symmetric tilt grain boundaries with the e structural unit. *Acta Mater.* **55**, 3959–3969 (2007).
- Tucker, G. J., Tschopp, M. A. & McDowell, D. L. Evolution of structure and free volume in symmetric tilt grain boundaries during dislocation nucleation. *Acta Mater.* **58**, 6464–6473 (2010).
- Sanzos, F. & Molinari, J. Mechanical behavior of Σ tilt grain boundaries in nanoscale Cu and Al: a quasicontinuum study. *Acta Mater.* **53**, 1931–1944 (2005).
- Anikeenko, A., Medvedev, N. & Aste, T. Structural and entropic insights into the nature of the random-close-packing limit. *Phys. Rev. E* **77**, 031101 (2008).
- Schoenholz, S. S., Cubuk, E. D., Kaxiras, E. & Liu, A. J. A structural approach to relaxation in glassy liquids. *Nat. Phys.* **12**, 469–471 (2016).
- Wolf, D. Correlation between energy and volume expansion for grain boundaries in fcc metals. *Scr. Metal.* **23**, 1913–1918 (1989).
- Fecht, H. J. Intrinsic instability and entropy stabilization of grain boundaries. *Phys. Rev. Lett.* **65**, 610–613 (1990).
- Shvindlerman, L. *et al.* Grain boundary excess free volume-direct thermodynamic measurement. *J. Mater. Sci.* **41**, 7725–7729 (2006).
- Buranova, Y., Rösner, H., Divinski, S. V., Imlau, R. & Wilde, G. Quantitative measurements of grain boundary excess volume from haadf-stem micrographs. *Acta Mater.* **106**, 367–373 (2016).
- Stukowski, A. Visualization and analysis of atomistic simulation data with ovito—the open visualization tool. *Model. Simul. Mater. Sci. Eng.* **18**, 015012 (2009).

60. Banadaki, A. D. & Patala, S. An efficient algorithm for computing the primitive bases of a general lattice plane. *J. Appl. Crystallogr.* **48**, 585–588 (2015).



Open Access This article is licensed under a Creative Commons Attribution 4.0 International License, which permits use, sharing, adaptation, distribution and reproduction in any medium or format, as long as you give appropriate credit to the original author(s) and the source, provide a link to the Creative Commons license, and indicate if changes were made. The images or other third party

material in this article are included in the article's Creative Commons license, unless indicated otherwise in a credit line to the material. If material is not included in the article's Creative Commons license and your intended use is not permitted by statutory regulation or exceeds the permitted use, you will need to obtain permission directly from the copyright holder. To view a copy of this license, visit <http://creativecommons.org/licenses/by/4.0/>.

© The Author(s) 2017

Supplementary Information accompanies the paper on the *npj Computational Materials* website (doi:[10.1038/s41524-017-0016-0](https://doi.org/10.1038/s41524-017-0016-0)).